JOURNAL OF COMPUTATIONAL PHYSICS **145,** 489–510 (1998)
ARTICLE NO. CP986040

A Numerical Study Comparing Kinetic Flux–Vector Splitting for the Navier–Stokes Equations with a Particle Method

T. Lou, D. C. Dahlby, and D. Baganoff[1]

Department of Aeronautics and Astronautics, Stanford University, Stanford, California 94305
E-mail: baganoff@hpsim.stanford.edu

Received March 28, 1997; revised April 28, 1998

Numerical solutions based on the method of kinetic flux-vector splitting (KFVS) for the Navier–Stokes equations are compared with results from the direct simulation Monte Carlo method (DSMC) for three problems: an impulsively started piston, which emphasizes heat flux; an impulsively started flat plate, which emphasizes shearing stress; and a plate sliding past a square cavity, or the lid-driven cavity problem, which combines both stress and heat flux. Taking the view that the DSMC method provides the correct physical description near material boundaries, the comparisons which were carried out for the conditions of a slightly rarefied flow show good agreement for temperature slip, velocity slip, and in the prediction of the kinetic split fluxes, verifying the assumptions and the approach taken in the development of the KFVS method.

Key Words: gas-kinetic scheme; flux-splitting; Navier–Stokes; flux boundary conditions.

I. INTRODUCTION

The theoretical development for the method of kinetic flux-vector splitting (KFVS) for the Navier–Stokes equations was introduced in Ref. [4], which represents an extension of work with the Euler equations initiated by Pullin [10] and further developed by Mandal and Deshpande [6,7]. Additionally, KFVS was shown for several sample problems to give good agreement with established numerical schemes for the Navier–Stokes equations. Boundary conditions based on the new split fluxes and the kinetic theory were also developed in [4] and shown to predict slip (first order) at a material surface, as a gas becomes rarefied.

[1] Corresponding author.

0021-9991/98 $25.00

However, confirmation for the magnitude of the predicted slip and the conditions under which the correct predictions are found were not fully explored. Also not given was support for the use of a critical approximation, based on the Eucken model, which was introduced to carry out the flux-splitting for energy, in the case of a gas having internal structure. The objective of the present work is to provide the appropriate analysis by comparing the predictions of the theory presented in [4] with the results of simulations carried out with the direct simulation Monte Carlo (DSMC) method [2,3], a method of simulation where a large collection of particles is used to model a rarefied gas flow. Of course, the comparisons can only be carried out in the near-continuum regime, where the computational cost for the DSMC method does not become prohibitive. Likewise, for the KFVS equations to hold the flow should only be slightly rarefied and the magnitudes of stress and heat flux must lie in a range where the occurrence of slip near a solid surface represents the principal modification to the fluid physics (first-order slip). However, these conditions are wholly consistent with the objective in [4], where the KFVS method was introduced as the continuum counterpart to the DSMC method in an eventual construction of a hybrid scheme combining the two.

The version of the DSMC method used in this study [1,8] divides space into uniform cubical cells. These cells are used to identify which particle pairs are candidates for collision during a time step and to compute cell-averaged macroscopic quantities at the end of a time step. In general terms, the DSMC method is expected to give reliable results when the local mean-free path length is large, compared with the cell dimension. Particular experience with the case of Couette flow has shown that good agreement for viscous stress and heat flux is obtained between DSMC and NS when the cell Knudsen number is greater than unity, and progressively more modest agreement is found as it is made smaller [5]. In our comparisons, the local cell Knudsen number appearing in the DSMC simulations approached unity only for a single cell and flow condition studied. The molecular model chosen for the simulations was the hard-sphere molecule, for which the transport coefficients vary as the square root of the temperature. In the case of a diatomic gas, the vibrational mode was not excited, while the rotational degrees of freedom were set to be in equilibrium with the translational degrees of freedom, by setting the so-called collision number in DSMC to unity. In the simulation, this leads to the ideal diatomic gas for which $\gamma = 7/5$.

Two issues are addressed in this study: (i) in the case of a simple gas, the theory in [4] is rather securely founded, and therefore, the primary question relates to whether the magnitude of the predicted slip for the particular flow conditions considered is in agreement with results obtained from DSMC simulations; and (ii) in the case of a gas with internal structure, the flux-splitting employed in [4] is based on the Eucken approximation, which directly affects the predicted split energy fluxes, and the particular approximation used requires confirmation, especially at or near a material surface where nonequilibrium effects may be large. These questions will be investigated by studying the highly nonequilibrium flow produced near material surfaces for three problems: an impulsively started piston, which emphasizes heat flux; an impulsively started flat plate, which emphasizes shearing stress; and a plate sliding past a square cavity, or the lid-driven cavity problem, which combines both stress and heat flux as important quantities.

As will be seen below, one of the principal benefits of the KFVS formulation is that it not only leads to a solution of the NS equations but it is also able to account for slip boundary conditions in a natural way which correspond precisely to the first-order slip boundary conditions studied by Patterson [9]. Alternatively, if one were interested in no-slip boundary conditions then these, too, can be applied. As a result, it is convenient to

regard KFVS and NS as equivalent systems, with KFVS having somewhat greater flexibility in the specification of boundary conditions. In addition, it should be noted that the introduction of first-order slip leads to a near-continuum theory and does not capture the full physics of the well-known Knudsen layer studied in kinetic theory, which lies within a distance of several mean-free path lengths from a material surface. Thus, in comparisons with the DSMC method, the two approaches are not expected to precisely agree in every measure in the immediate vicinity of a material surface, as only the DSMC method is capable of capturing the correct physics.

II. THE KFVS EQUATIONS

The split kinetic fluxes for the Navier–Stokes equations are given by Eqs. (39)–(44) in Ref. [4] and these are reproduced for use here, where the notation employed is the same and they read

$$F^{\pm}_{\text{mass}} = \rho\sqrt{RT/2}[(1\pm\alpha_1)S_n \pm \alpha_2(1-\chi_1)] \tag{1}$$

$$F^{\pm}_{n-\text{mom}} = p\left[(1\pm\alpha_1)\left(S_n^2 + \frac{1}{2}\left(1-\hat{\tau}^{CE}_{nn}\right)\right) \pm \alpha_2\left(S_n + \hat{q}^{CE}_n\right)\right] \tag{2}$$

$$F^{\pm}_{t1-\text{mom}} = \sqrt{2RT}\left[S_{t1}F^{\pm}_{\text{mass}}\right] + \frac{1}{2}p\left[-(1\pm\alpha_1)\hat{\tau}^{CE}_{nt1} \pm \alpha_2\hat{q}^{CE}_{t1}\right] \tag{3}$$

$$F^{\pm}_{tr-\text{energy}} = p\sqrt{RT/2}\left[(1\pm\alpha_1)\left(S_n\left(\frac{5}{2}+S^2\right)+\chi_2\right) \pm \alpha_2\left(2+S^2+\chi_3\right)\right] \tag{4}$$

$$F^{\pm}_{\text{int}-\text{energy}} = \frac{1}{2}\left(\frac{5-3\gamma}{\gamma-1}\right)\left[RTF^{\pm}_{\text{mass}}\right] \tag{5}$$

$$F^{\pm}_{\text{energy}} = F^{\pm}_{tr-\text{energy}} + F^{\pm}_{int-\text{energy}}, \tag{6}$$

where

$$\alpha_1 = erf(S_n), \quad \alpha_2 = \frac{1}{\sqrt{\pi}}e^{-S_n^2}$$

$$\chi_1 = \left[S_n\hat{q}^{CE}_n + \frac{1}{2}\hat{\tau}^{CE}_{nn}\right]$$

$$\chi_2 = \left[\frac{5}{2}\hat{q}^{CE}_n - \left(S_n\hat{\tau}^{CE}_{nn} + S_{t1}\hat{\tau}^{CE}_{nt1} + S_{t2}\hat{\tau}^{CE}_{nt2}\right)\right]$$

$$\chi_3 = \left[S_{t1}\hat{q}^{CE}_{t1} + S_{t2}\hat{q}^{CE}_{t2} - \chi_1\left(1+S_{t1}^2+S_{t2}^2\right) - \hat{\tau}^{CE}_{nn}\right]$$

$$S_n = u_n/\sqrt{2RT}, \quad S^2 = S_n^2 + S_{t1}^2 + S_{t2}^2$$

$$\hat{\tau}^{CE}_{nn} = \tau^{CE}_{nn}/p, \qquad \hat{q}^{CE}_n = \frac{2}{5}q^{CE}_n/(p\sqrt{2RT})$$

$$q^{CE}_i = -K^{(1)}\frac{\partial T}{\partial x_i}$$

$$\tau^{CE}_{ij} = \mu^{(1)}\left(\frac{\partial u_i}{\partial x_j} + \frac{\partial u_j}{\partial x_i}\right) - \frac{2}{3}\mu^{(1)}\left(\frac{\partial u_k}{\partial x_k}\right)\delta_{ij}.$$

A Cartesian coordinate system is assumed in the above equations, with the normal direction represented by n, and the two tangential directions by $t1$ and $t2$. The dimensionless velocity S

(speed ratio) determines the two parameters α_1 and α_2, while the dimensionless, Chapman–Enskog expressions for stress $\hat{\tau}_{ij}^{CE}$ and heat flux $\hat{q}_n^{CE}$ are the nonequilibrium factors in the quantities χ_1, χ_2, and χ_3. The sign convention employed assumes the positive split flux F^+ points in the direction of increasing n and is directed out of a surface enclosing a body of gas. The convention for F^- is based on the splitting $F = F^+ + F^-$, where F is the total flux, and therefore F^- often evaluates to a negative value. The corresponding expression for $F^{\pm}_{t2-\mathrm{mom}}$ is not listed as it can be inferred from (3).

Extreme nonequilibrium conditions in a gas are found near isothermal boundaries, where the one-sided fluxes are large, and these provide unique conditions for detailed study. The relations developed for an isothermal boundary are given by Eqs. (63)–(66) in Ref. [4] and these are also listed below, where again the same notation is followed,

$$\left(F^+_{\mathrm{mass}}\right)_{\mathrm{g}} = \rho_{\mathrm{w}}\sqrt{RT_{\mathrm{w}}/2\pi}, \tag{7}$$

$$(F_{n-\mathrm{mom}})_{\mathrm{surface}} = \left(F^+_{n-\mathrm{mom}}\right)_{\mathrm{g}} + p_{\mathrm{w}}/2, \tag{8}$$

$$(F_{t1-\mathrm{mom}})_{\mathrm{surface}} = \left(F^+_{t1-\mathrm{mom}}\right)_{\mathrm{g}}, \tag{9}$$

$$(F_{\mathrm{energy}})_{\mathrm{surface}} = \left(F^+_{\mathrm{energy}}\right)_{\mathrm{g}} - p_{\mathrm{w}}\sqrt{2RT_{\mathrm{w}}/\pi}\left[1 + \frac{1}{4}\left(\frac{5-3\gamma}{\gamma-1}\right)\right]. \tag{10}$$

In the above relations, the state of the gas near a surface is denoted by subscript g, while the state of the hypothetical wall gas is denoted by subscript w. These relations were developed in [4] using DSMC type boundary conditions for a nonreacting gas, in which the wall can be viewed as a hypothetical gas at conditions determined by the particular boundary conditions employed. In this case, the wall gas is the same gas because of the assumed nonreacting interaction between gas molecules. Likewise, the sign convention assumed in the boundary conditions (7)–(10) is one where a positive flux points in the direction of positive n (into the wall), when viewed from the position of the gas at an interface with a wall.

III. IMPULSIVELY STARTED PISTON

The interest in an impulsively started piston is associated with the fact that the heat transfer rate to an isothermal piston can be very high at early time, leading to large nonequilibrium effects. On the other hand, the impulsive start requires special attention, as will be seen. Because it is not obvious from the structure of Eqs. (7)–(10) how the condition of zero slip is recovered in the continuum limit, and because DSMC simulations become overly costly in this limit, it is desirable to further develop the theoretical expressions so that comparisons can be more readily assessed. The continuum limit is obtained for conditions of high density and large time when the boundary layer is relatively thick in relation to the local mean free path length. For the one-dimensional geometry of an impulsively started piston, where the $t1$ and $t2$ coordinates are ignored, this leads to small values of the surviving dimensionless derivatives $\hat{\tau}_{nn}^{CE}$ and $\hat{q}_n^{CE}$, generally with $\hat{\tau}_{nn}^{CE} \ll \hat{q}_n^{CE}$. For calculational purposes, it is easier to consider a moving gas and a stationary piston, and therefore, at the piston surface it is appropriate to set the speed ratio to zero, i.e. $S_n = 0$. Thus, $\alpha_1 = 0$ and $\alpha_2 = 1/\sqrt{\pi}$. On using (1) to represent the gas near a surface and on using boundary condition (7), the following relations between the conditions in the gas flow and the hypothetical wall-gas values are obtained:

$$\frac{\rho_{\mathrm{g}}}{\rho_{\mathrm{w}}}\left(1 - \frac{1}{2}\tilde{\tau}_{nn}^{CE}\right) = \sqrt{\frac{T_{\mathrm{w}}}{T_{\mathrm{g}}}}, \quad \frac{p_{\mathrm{g}}}{p_{\mathrm{w}}}\left(1 - \frac{1}{2}\tilde{\tau}_{nn}^{CE}\right) = \sqrt{\frac{T_{\mathrm{g}}}{T_{\mathrm{w}}}}, \tag{11}$$

where $p = \rho RT$ is used for both the gas flow and the hypothetical wall gas. When Eqs. (4)–(6) are substituted into boundary condition (10) and on making use of (11) we obtain for the total energy flux at the surface the relation

$$\frac{4(F_{\text{energy}})_{\text{surface}}}{p_{\text{g}}\sqrt{2RT_{\text{g}}}} = 5\hat{q}_n^{CE} + \frac{1}{\sqrt{\pi}}\left(\frac{\gamma+1}{\gamma-1}\right)\left(1-\frac{T_{\text{w}}}{T_{\text{g}}}\right) - \frac{1}{2\sqrt{\pi}}\left[\left(\frac{3\gamma-1}{\gamma-1}\right) - \left(\frac{\gamma+1}{\gamma-1}\right)\left(\frac{T_{\text{w}}}{T_{\text{g}}}\right)\right]\hat{\tau}_{nn}^{CE}. \tag{12}$$

The definition for the total energy flux in the coordinate system for which $S_n = 0$ simplifies to the relation $(F_{\text{energy}})_{\text{surface}} = q_n^{CE}$, and consequently, the above equation reduces to

$$\left(1-\frac{1}{2}\hat{\tau}_{nn}^{CE}\right)\frac{T_w}{T_g} = 1 - 5\sqrt{\pi}\left(\frac{\gamma-1}{\gamma+1}\right)\hat{q}_n^{CE} - \frac{1}{2}\left(\frac{3\gamma-1}{\gamma+1}\right)\hat{\tau}_{nn}^{CE}. \tag{13}$$

For an isothermal piston, heat conduction represents the dominant effect at large time. Therefore, the above equation can be approximated for $\hat{\tau}_{nn}^{CE} \ll 1$ by

$$\frac{T_{\text{w}}}{T_{\text{g}}} = 1 - \left(\frac{\gamma-1}{\gamma+1}\right)\left(5\sqrt{\pi}\hat{q}_n^{CE} + \hat{\tau}_{nn}^{CE}\right) \tag{14}$$

which shows that the gas temperature near the surface T_{g} approaches the wall temperature T_{w}, as the magnitudes of the nonequilibrium parameters become smaller and smaller in approaching the continuum limit (because of the presence of p in the definitions of $\hat{\tau} = \tau/p$ and $\hat{q} = q/pc$). For positive heat flux, i.e. heat flux directed towards the wall, the gas temperature is greater than the wall temperature. An entirely equivalent first-order slip condition for the case of slightly rarefied flow of a monatomic gas was obtained by Patterson and it is easy to show that Eq. (14) fully agrees with Patterson's result (Ref. [9, Eq. (33), p. 125]). This agreement is found on setting $\gamma = 5/3$, Prandtl number $= 2/3$, and then approximating (14) for the inverted ratio $T_{\text{g}}/T_{\text{w}}$. Additionally, it has been shown by Shidlovskiy [11], again for the case of a monatomic gas, that inclusion of the thermal accommodation coefficient α introduces a factor $(2-\alpha)/\alpha$ multiplying the heat flux term (Ref. [11, Eq. (3.16), p. 67]). Equation (14) was developed here for two purposes: to show that the KFVS formulation (1)–(6) and the associated boundary conditions (7)–(10) agree with related work and to introduce the extension to the case of a polyatomic gas.

Returning to the more descriptive view, where the gas and piston are both stationary and at one temperature before the start of the motion, then the larger the piston velocity after the impulsive start the larger the Mach number associated with the shock wave produced, and the greater the changes in density and temperature across the gas layer formed near the piston. When one employs the continuum (KFVS or NS) point of view, a discontinuity appears at the wall in both the temperature and the fluid velocity at time $t = 0^+$, and the corresponding heat flux and normal stress are infinite, and this occurs even for low values of the piston velocity. Clearly, the equations do not predict the correct physical process at very early time. This raises the interesting question for this nonsteady problem whether a numerical solution of the continuum equations for large time would be independent of developments at early time.

Because Eq. (14) is an analytic result which does not depend explicitly on time, it can be used to qualify a numerical solution of the KFVS equations, because one would expect (14) to provide the correct prediction as a numerical solution is sequentially improved. The

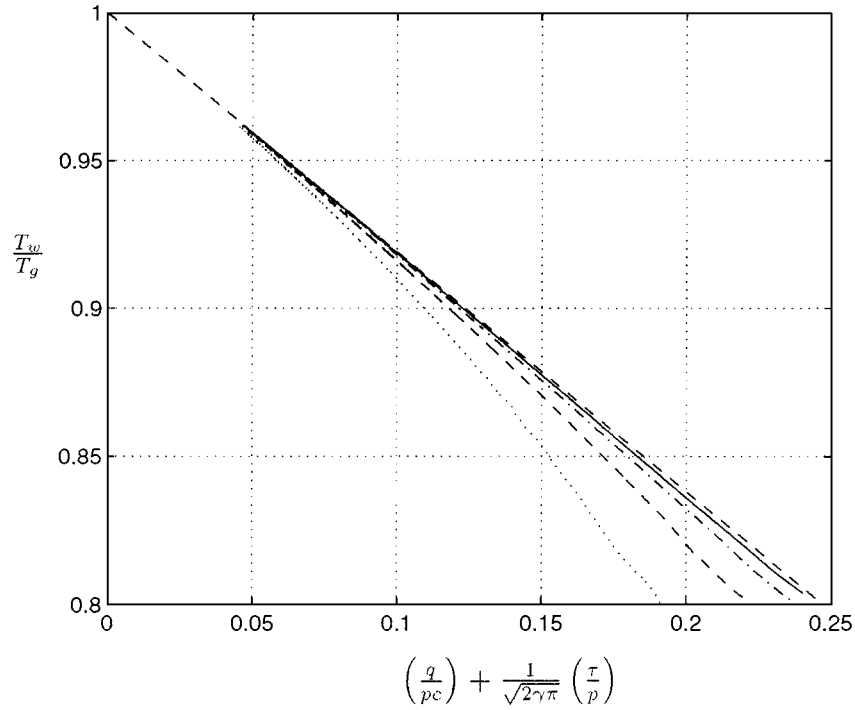

FIG. 1. Gas temperature at the surface of an impulsively started isothermal piston moving into a stationary monatomic gas. Theoretical relation given by Eq. (14) (- - - -). Numerical integration of the KFVS equations for $M_{piston} = 1$, $\gamma = 5/3$, and reference cell Knudsen number $Kn_0 = 2$ ($\cdots$); 4 (- - - -); 8 (- $\cdots$ -); and 16 (———).

need for a reliable numerical check is the principal reason why the temperature ratio in (14) was not inverted, i.e. to correspond more directly to Patterson's expression. On using the variables defined by Eq. (14), the analytical relation plots as a straight line, which is shown as a heavy dashed line in Fig. 1 (note: $q/pc = 5\hat{q}/\sqrt{2\gamma}$). The four numerical solutions shown in the figure were carried out for the case of a monatomic gas and a piston Mach number of unity ($M_{\text{shock}} = 1.869$), using a second-order finite-volume scheme (first-order time), together with a range of cell sizes (see Ref. [4] for identification of the scheme used). Time appears as a parameter along each curve, with large time corresponding to small values of the abscissa. The physical scale is set by the values of the undisturbed density ρ_0, speed of sound c_0, coefficient of viscosity μ_0, and cell length Δx. These quantities can either be used to define a reference cell Reynolds number or a reference cell Knudsen number through the kinetic-theory, hard-sphere relation.

$$\mu = \frac{5\pi}{32}\rho\bar{C}\lambda, \tag{15}$$

where $\bar{C} = \sqrt{8RT/\pi}$ is the mean thermal speed and λ is the mean free path length. Because we are interested in comparisons with DSMC, it is physically more meaningful to use a reference cell Knudsen number, $Kn_0 = \lambda_0/\Delta x$, with $\tilde{x} = x/\lambda_0$, $\tilde{t} = t\bar{C}_0/\lambda_0 = t/t_c$, and

$$\Delta\tilde{t} = \Delta t\bar{C}_0/\Delta x Kn_0 = \sqrt{\frac{8}{\pi\gamma}}\left(\frac{c_0\Delta t}{\Delta x}\right)\Big/ Kn_0, \tag{16}$$

as measures of the physical scale. The numerical solutions are shown for $Kn_0 = 2, 4, 8, 16$ and we see that the largest value is needed to get good agreement with (14) for $T_w/T_g > 0.8$. Because the gas density near the piston surface is nearly four times the undisturbed density (see Fig. 3), this translates into $Kn_{wall} \approx 4$ and therefore we must have $\Delta x < \lambda_{wall}/4$ to obtain a reliable solution at early time. The conditions near $t = 0^+$ necessitated the use of a very small $\Delta\tilde{t}$. This led to the use of values of $c_0\Delta t/\Delta x$ ranging from 0.15 to 0.0375 as the Knudsen number was increased. At this point we do not know whether the range of the independent variable displayed in Fig. 1 corresponds to conditions where the KFVS system predicts the correct physics, only that the values employed are required for a consistent numerical solution of the equations.

In turning to a DSMC simulation, it is clear that the same reference cell Knudsen number, $Kn_0 = 16$, should initially be used in making a comparison. Figure 2 shows such a

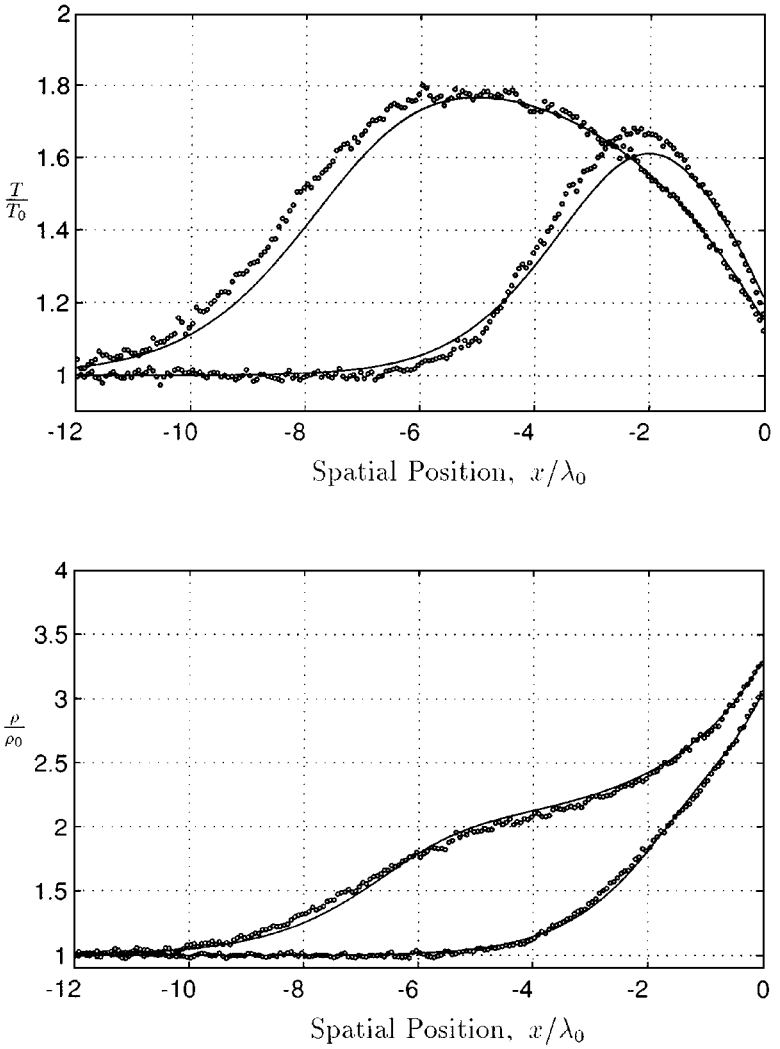

FIG. 2. Gas temperature and density ahead of an isothermal piston (located at $\tilde{x} = 0$) for KFVS (solid curves) and DSMC (symbols), at two early times in the formation of the shock wave and the thermal layer, for $M_{piston} = 1$ and $\gamma = 5/3$. Dimensionless times correspond to $\tilde{t} = 4.64$ and $\tilde{t} = 11.6$.

comparison for two times: a time at which the shock wave and the thermal layer are both still forming, $\tilde{t} = 4.64$ (1600 time steps KFVS, 400 DSMC); and the time at which they just begin to separate, $\tilde{t} = 11.6$ (4000 time steps KFVS, 1000 DSMC). Numerical instability with KFVS at early time necessitated a smaller time step (factor of 4) than that used with DSMC. The dimensionless time employed is based on the collision time in the reference state and so these times are truly short. At the early time the temperature profiles match somewhat poorly overall, while at the later time the thermal layers, as opposed to the shock layers, begin to match rather well. Because density is a less sensitive variable, the match at both times is surprisingly good, considering the extremely short time represented. Because the DSMC method is computationally intensive, it was necessary to increase the values of $\Delta\tilde{t}$ and Δx by a factor of 4 and to decrease the value of Kn_0 by the same factor to study still larger time. Figure 3 makes the same comparison after the shock wave and the thermal layer have clearly separated, $\tilde{t} = 46.4$ (16,000 time steps KFVS; 1000 DSMC), and it is seen that agreement is very good, except at the shock front itself for which it is well known that NS gives a poor prediction for the shock-wave profile.

The inherent statistical fluctuations which are characteristic of the DSMC method, especially for a nonsteady problem for which extended time averaging is not possible, does not allow for a detailed study of small differences represented by the temperature slip seen in Figs. 2 and 3. Nevertheless, in Fig. 4 we attempt to make a comparison of the time dependent temperature slip at the piston surface for the two methods. In this case, the DSMC results were time averaged over a small local interval about each plotted point to reduce statistical scatter. These simulations were carried out with a number density of approximately 8000 particles per cell near the piston surface and roughly one million particles for the entire simulation. DSMC results were obtained for $Kn_0 = 4, 8, 16, 32$ by sequentially reducing the cell size by a factor of 2 while holding λ_0 fixed. These data include the runs shown in Figs. 2 and 3, and likewise are for the same conditions. Because of the varying cell size, it would be necessary to extrapolate the data for each run to the position of the piston surface in order to produce a consistent display, but this approach amplifies statistical scatter and proves impractical for a time-dependent simulation with DSMC. The alternative was to select the center position of the largest DSMC cell ($Kn_0 = 4$) as the reference and display the data for all runs for that position. This approach has the added feature that it provides a consistency check on the DSMC method itself. As seen in Fig. 4, the DSMC data for different cell sizes overlap nicely, demonstrating that convergence has been obtained. Two curves are shown for the KFVS calculation: the dashed curve was obtained by extrapolating the data to the piston surface; and the solid curve represents the value at the center position of the largest cell used in the DSMC method ($Kn_0 = 4$). For the KFVS calculation, the cell size for $Kn_0 = 16$ was used. The separation between the two curves shows that the temperature gradient near the piston surface is very steep, necessitating the use of a very small cell size. In view of the different curves displayed, the solid curve for KFVS should be compared with the DSMC data, which appears to suggests that the boundary conditions (7)–(11) for KFVS slightly overpredict the temperature slip for these conditions. For large time the two should agree fully, but it did not appear feasible to extend the DSMC runs to verify this with the computer workstation employed in this part of the study. When considering the fact that the NS equations are not expected to represent the correct physics for large nonequilibrum (for example, $q/pc > 0.1$ for $\tilde{t} < 50$, as found from Figs. 1 and 4), the agreement seen in Figs. 2–4 is very encouraging, since it confirms the accepted view that slip conditions at a surface represent the principal corrections needed to be added to the NS system when dealing with a slightly rarefied flow.

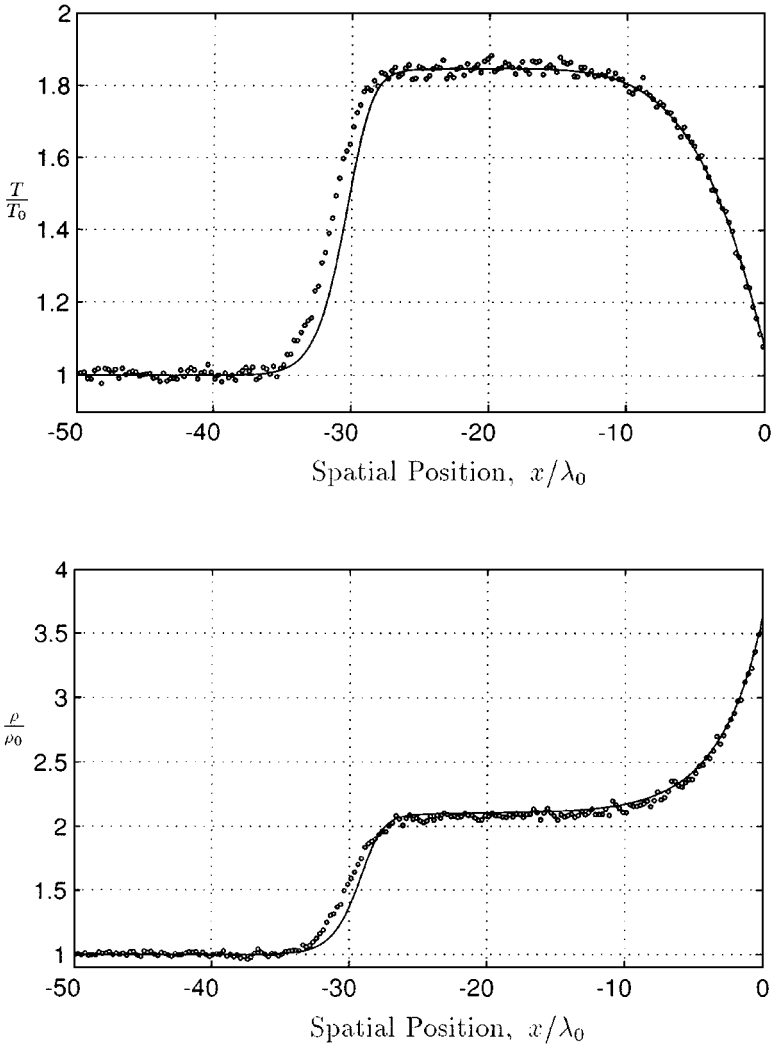

FIG. 3. Gas temperature and density ahead of an isothermal piston (located at $\tilde{x} = 0$) for KFVS (solid curves) and DSMC (symbols), for $M_{piston} = 1$, $\gamma = 5/3$, and at a time $\tilde{t} = 46.4$ when the shock wave and thermal layer have clearly separated, showing a well-defined thermal layer. The DSMC results are for $Kn_0 = 4$ while the KFVS results are for $Kn_0 = 16$, i.e., Δx for KFVS is four times smaller than for DSMC.

If any discrepancy exists between the values of the split kinetic fluxes defined by Eqs. (1)–(6) and the corresponding values from DSMC simulations, then the differences should be seen at the piston surface where nonequilibrium is the greatest. Figure 5 presents the corresponding comparisons for the mass and energy split fluxes and shows that the agreement for a monatomic gas is extremely good. In the DSMC simulations the positive split fluxes were obtained by monitoring the passage of individual particles as they left the gas and crossed the piston surface, while the negative split fluxes were obtained by monitoring the particle emission from the piston surface introduced by the DSMC boundary conditions. For the KFVS solution the state of the flow from the numerical solution was used to evaluate the positive split fluxes using the defining equations (1)–(6). Similarly, the conditions representing the isothermal piston were used to compute the negative split fluxes.

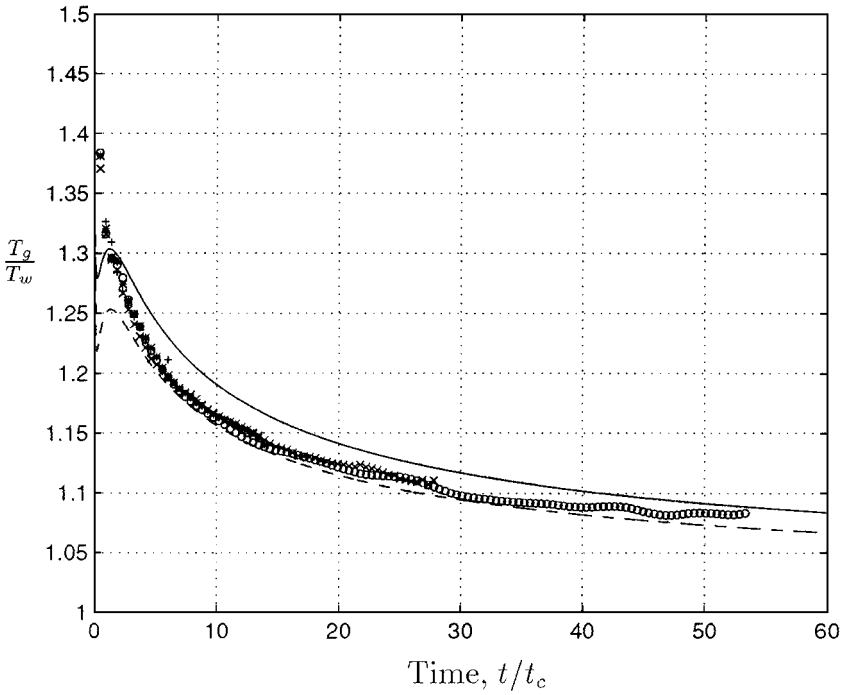

FIG. 4. Gas temperature at the surface of an isothermal piston versus dimensionless time, for $M_{piston} = 1$ and $\gamma = 5/3$. DSMC cell dimensions correspond to $Kn_0 = 2$ (○); 4 (×); 8 (∗); 16 (+). The KFVS solution was evaluated for $Kn_0 = 16$ and projected to the piston surface (dashed curve); same solution was evaluated at cell center for the largest DSMC cell (solid curve).

In the case of a polyatomic gas, the Eucken approximation was introduced in [4] to develop the split fluxes for energy; and it is of interest to determine whether the particular approximation used is supported by DSMC. The same simulations were repeated for the case of an ideal diatomic gas, assuming rotational degrees of freedom are in equilibrium with translation ($\gamma = 7/5$), and a comparison of split fluxes for momentum and energy are shown in Fig. 6. The excellent agreement seen confirms that the Eucken approximation, as implemented in [4], is capturing the proper physics in the splitting of energy flux for both the translational and rotational components.

IV. IMPULSIVELY STARTED FLAT PLATE

Viscous stress becomes the dominant nonequilibrium effect for an impulsively started flat plate, which provides an alternate environment for comparison. For the one-dimensional geometry of an infinite, impulsively started flat isothermal plate moving parallel to its surface in, say, the t_1 direction, the t_1 and t_2 coordinates may be disregarded in (1)–(6); and the shearing stress $\hat{\tau}_{nt1}^{CE}$, along with the normal heat-flux component $\hat{q}_n^{CE}$, become the principal nonequilibrium quantities. Again, for calculational purposes it is easier to consider a moving gas and a stationary plate. At the plate surface we may then set $S_n = 0$ and thus $\alpha_1 = 0$ and $\alpha_2 = 1/\sqrt{\pi}$. On using Eq. (1) to represent the gas near the plate and on using boundary condition (7), exactly the same density and temperature relations are found as for the impulsively started piston, given by (11).

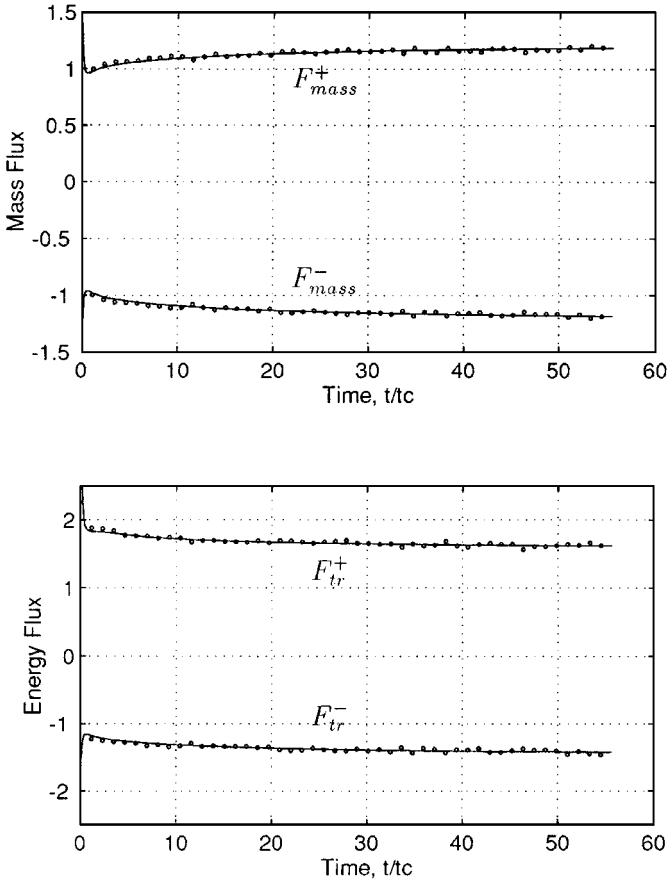

FIG. 5. Kinetic split fluxes evaluated at the surface of an isothermal piston, for $M_{piston} = 1$ and $\gamma = 5/3$. The numerical solution of the KFVS equations (solid curves) are compared with results from a DSMC simulation (symbols). Mass and energy split fluxes are referenced to the values $\rho_0 c_0$ and $\rho_0 c_0^3$, respectively.

On using (1) and (3) to represent the gas near a stationary surface, in which we set $\hat{q}^{CE}_{t1}$ to zero because of uniformity, and on using boundary condition (9), we find

$$(F_{t1-\mathrm{mom}})_{\mathrm{surface}} = \left[\frac{1}{\sqrt{\pi}} p S_{t1}\left(1 - \frac{1}{2}\hat{\tau}^{CE}_{nn}\right) - \frac{1}{2} p \hat{\tau}^{CE}_{nt1}\right]_g . \tag{17}$$

The definition for the total flux of transverse momentum leads to the substitution $(F_{t1-\mathrm{mom}})_{\mathrm{surface}} = -\tau_{nt1}$, because $S_n = 0$. On solving for S_{t1}, we then obtain the relation

$$S_{t1} = -\frac{\sqrt{\pi}}{2}\left(1 - \frac{1}{2}\hat{\tau}^{CE}_{nn}\right)^{-1} \hat{\tau}^{CE}_{nt1}. \tag{18}$$

The quantity S_{t1} represents the dimensionless velocity of the fluid next to a stationary surface, i.e. velocity slip. Although Eq. (18) does not depend directly on the value of the ratio of specific heats γ, however, if the velocity slip is based on the reference plate speed u_{plate} and a plate Mach number M_{plate} is introduced, then the factor $\sqrt{\pi}/2$ is replaced by $\sqrt{\pi/2\gamma}/M_{\mathrm{plate}}$ and a γ dependence becomes evident. Here again, if we neglect $\hat{\tau}^{CE}_{nn}$ then the

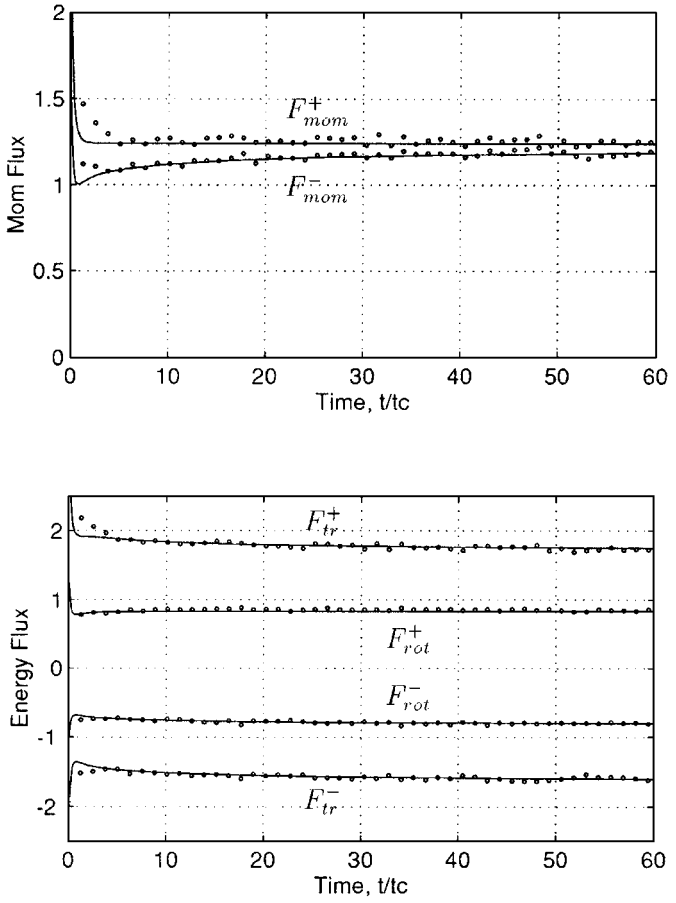

FIG. 6. Kinetic split fluxes evaluated at the surface of an isothermal piston, for $M_{piston} = 1$ and $\gamma = 7/5$. The numerical solution of the KFVS equations (solid curves) are compared with results from a DSMC simulation (symbols). Momentum and energy split fluxes are referenced to the values $\rho_0 c_0^2$ and $\rho_0 c_0^3$, respectively.

above relation can be shown to agree fully with Patterson's result for velocity slip (Ref. [9, Eq. (31), p. 125]). If boundary condition (10) is handled in the same way as for the piston, and if the quadratic terms $S_{t1}\hat{\tau}_{nt1}$ and S_{t1}^2 are dropped, then exactly the same relation for the temperature slip as for the impulsively started piston is gotten, i.e. Eq. (14).

Just as for the case of the impulsively started piston, Eq. (18) can be used to qualify a numerical solution of the KFVS equations for an impulsively started flat plate. Except for a greater sensitivity to the impulsive start, which requires the use of still smaller time steps as the reference cell Knudsen number is increased, the conclusions drawn are essentially the same as those found in the study that led to the data presented in Fig. 1 and will not be repeated. Likewise, in order to emphasize nonequilibrium effects, an isothermal plate and a Mach number of unity were selected as appropriate conditions for study.

Using the more descriptive frame of reference where the gas is initially stationary and the plate is given an impulsive start, KFVS and DSMC results for velocity are displayed and compared in Fig. 7 for the dimensionless times $\tilde{t} = 12.4$ and $\tilde{t} = 68.0$. As can be seen, even though the velocity slip is fairly large at these short times, the KFVS solution compares extremely well with the DSMC results. It is also of interest to make comparisons with the

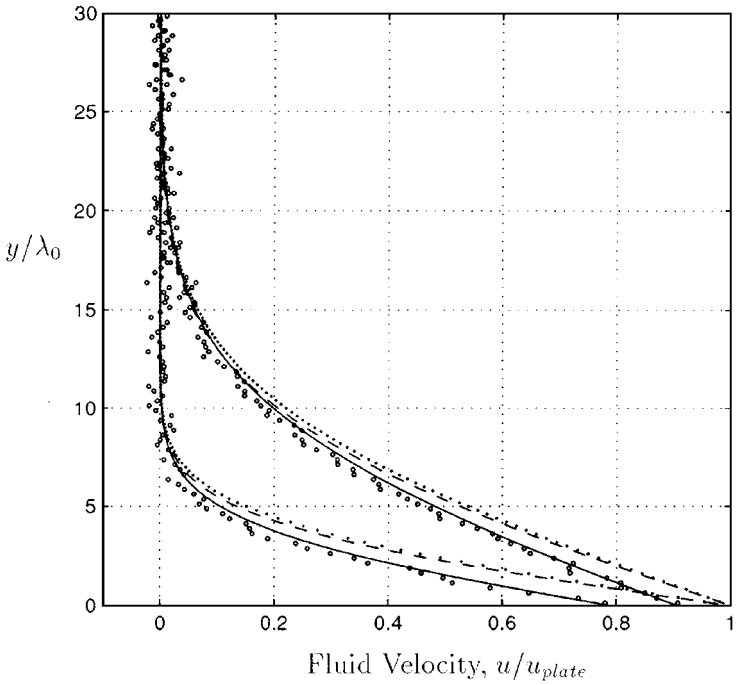

FIG. 7. Velocity distribution above an impulsively started isothermal flat plate, for $M_{plate} = 1$ and $\gamma = 5/3$. The two times shown are for $\tilde{t} = 12.4$ and 68.0, with KFVS (solid curves), DSMC (symbols), no-slip KFVS (dashed curves), and no-slip incompressible (dotted curves) displayed.

corresponding KFVS solution for no-slip boundary conditions identified in the figure by the dashed curves. Because the peak density and temperature variations are small (4% and 9%, respectively), it is reasonable to assume that the velocity can be approximated by the exact incompressible solution given by $u/u_p = 1 - \mathrm{erf}(\eta)$, where $\eta^2 = y^2/4\nu t = 8\tilde{y}^2/5\pi\tilde{t}$. This solution is shown by the dotted curves, which provide confidence that the numerical method used is capable of handling the impulsive start. In Fig. 8 the gas velocity at the surface of the plate is displayed as a function of time, showing that it approaches the plate velocity asymptotically. The DSMC results were obtained for $Kn_0 = 4$ and 8; and data for both runs were plotted for the location corresponding to the center position of the largest cell, $Kn_0 = 4$. The complete overlap of the symbols clearly demonstrates consistency, or convergence, in the DSMC results. In the case of the KFVS solution, the data for $Kn_0 = 12$ were used and extrapolated to the plate surface (dashed curve); the data were also evaluated at the center position of the largest cell (solid curve) used in the DSMC simulations. As the gradient near the plate is more modest here, the agreement is sufficiently close that one does not have to distinguish between the different curves. Equation (18) shows that the magnitude of $\hat{\tau}_{nt1}^{CE}$ is virtually the same as the slip $(1 - u/u_{\mathrm{plate}})$ seen in the figure. Therefore, the degree of nonequilibirum is quite large, yet the prediction for velocity slip agrees very nicely with DSMC for these rather extreme conditions.

Continuing with comparisons for the split kinetic fluxes evaluated at the plate surface, Fig. 9 presents the results for the case of a monatomic gas, and the agreement seen is remarkably good. The corresponding KFVS solution for no-slip boundary conditions is shown by the dashed curves. In this case the difference between slip and no-slip is significant. However, when the exact incompressible solution was used to compute the same

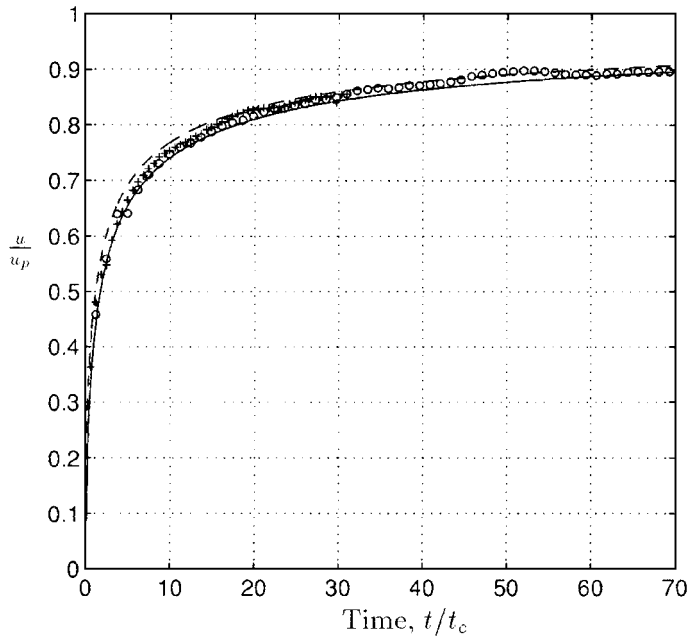

FIG. 8. Gas velocity at the surface of an impulsively started isothermal flat plate versus time, for $M_{plate} = 1$ and $\gamma = 5/3$. KFVS solution is for $Kn_0 = 12$ with extrapolation to surface (dashed curve) and location at cell center for largest DSMC cell (solid curve). DSMC simulation is for $Kn_0 = 4$ (○); 8 (+).

fluxes, the results superposed directly on the no-slip KFVS curves, confirming that the difference seen is real. Likewise, Fig. 10 presents the split fluxes for a diatomic gas, showing equally good agreement. These quantities are displayed for a frame of reference where the gas is initially stationary and the plate is given an impulsive start. Therefore, asymptotic results deduced from Eqs. (1)–(6) must be transformed to obtain the limiting values seen in Figs. 9 and 10. Beyond the excellent comparisons seen, the most important observation relates to the component quantities making up the energy split fluxes for the diatomic gas. It is clear that the translational and rotational degrees of freedom are being properly handled, and therefore, the approach used in Ref. [4], in introducing the Eucken approximation, appears to be working well.

V. LID-DRIVEN CAVITY FLOW

In the two cases studied above, heat flux and viscous stress were separately dominant; but both can become important in the lid-driven cavity problem, and an element of complexity is added by the two dimensions of the flow. However, focus will be placed on the steady-state condition for which the CFL restriction should not be as severe as for the case of an impulsive start. Here again, it is useful to assume isothermal surfaces to produce a large degree of nonequilibrium. On the other hand, the lid Mach number was set to $M_{lid} = 0.5$ so that nonequilibrium effects in the corners for steady state were not unduly large. The reference Knudsen number, based on the dimension of the square cavity L and defined by $Kn_L = \lambda_0/L$, was set equal to 0.01, where λ_0 is the mean-free path-length evaluated at the wall temperature and the initial state of the gas. The value of the Knudsen number was chosen so as to correspond to the near-continuum regime, where NS is expected to be valid

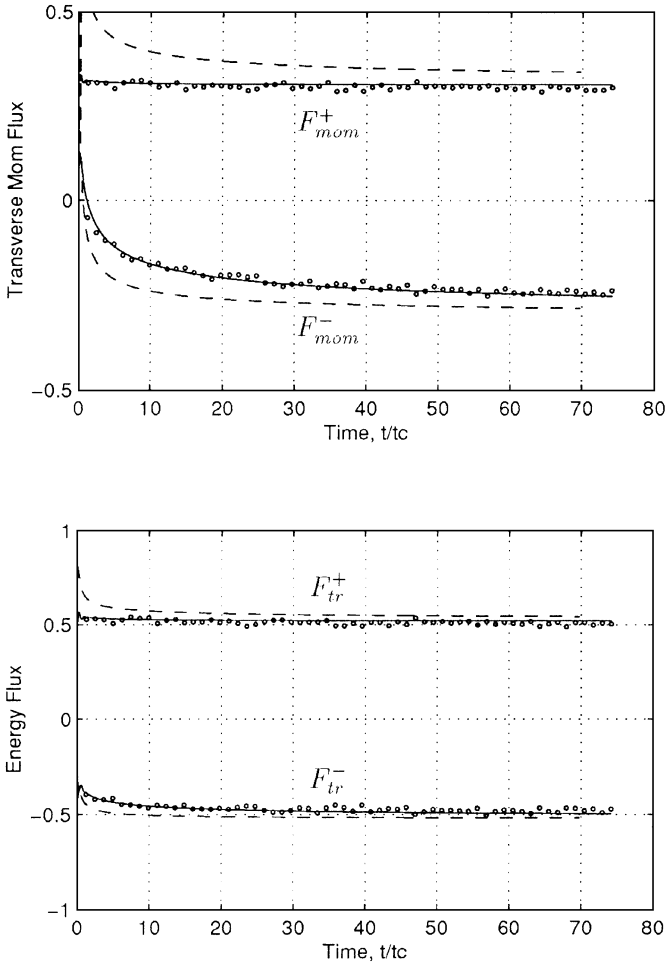

FIG. 9. Kinetic split fluxes evaluated at the surface of an isothermal flat plate, for $M_{plate} = 1$ and $\gamma = 5/3$. The numerical solution of the KFVS equations (solid curves) are compared with results from a DSMC simulation (symbols) and no-slip KFVS (dashed curves). Momentum and energy split fluxes are referenced to the values $\rho_0 c_0^2$ and $\rho_0 c_0^3$, respectively.

and the DSMC simulation does not become overly intensive. In the following, discussion will be limited to the case of a diatomic gas, as the monatomic case has been adequately covered above.

A steady-state, two-dimensional KFVS solution, based on a 128×128 square mesh, is presented in Fig. 11, showing the component of velocity lying parallel to the lid. In the figure, the lid is on the near face and moves from left to right for which the velocity is defined to be negative. The effect of velocity slip is clearly seen, both on the lid itself and at the two corners formed by the lid and walls. No slip would correspond to the magnitude of the dimensionless fluid velocity u/c_0 being equal to the lid Mach number in this case 0.5. The view shown is useful in serving as a mental aid in presenting the comparisons to be reviewed below. For example, in the views that follow the lid, together with the two faces on either side, will be unwrapped and displayed in planar form when various boundary quantities are compared.

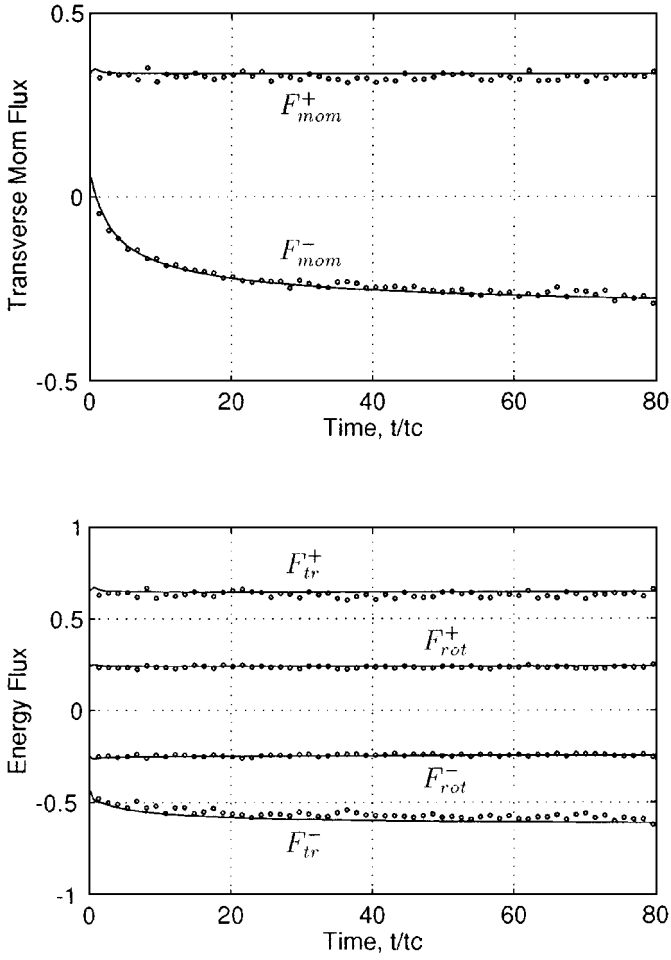

FIG. 10. Kinetic split fluxes evaluated at the surface of an isothermal flat plate for $M_{plate} = 1$ and $\gamma = 7/5$. The numerical solution of the KFVS equations (solid curves) are compared with results from a DSMC simulation (symbols). Momentum and energy split fluxes are referenced to the values $\rho_0 c_0^2$ and $\rho_0 c_0^3$, respectively.

In order to judge the validity of the numerical solution presented in Fig. 11, analytical relations similar to Eqs. (14) and (18) are needed. Using a coordinate system where n is taken to be perpendicular to the lid, $t1$ is parallel to the lid and $t2$ is ignorable, then at various points along the lid one would expect the stresses τ_{nt1}^{CE} and τ_{nn}^{CE} and the heat flux components q_n^{CE} and q_{t1}^{CE} to be important. On this basis the slip relations found above may have to be generalized. When the algebra leading to Eq. (11) is repeated using $S_n = 0$ alone, exactly the same relations are found. A slight generalization to (18) is required, given by

$$S_{t1} = -\left(1 - \frac{1}{2}\hat{\tau}_{nn}^{CE}\right)^{-1}\left[\frac{\sqrt{\pi}}{2}\hat{\tau}_{nt1}^{CE} + \frac{1}{2}\hat{q}_{t1}^{CE}\right], \tag{19}$$

which introduces the heat flux component aligned with the lid, a quantity that may be important in the corners. More terms must be retained in the generalization of (13) for the

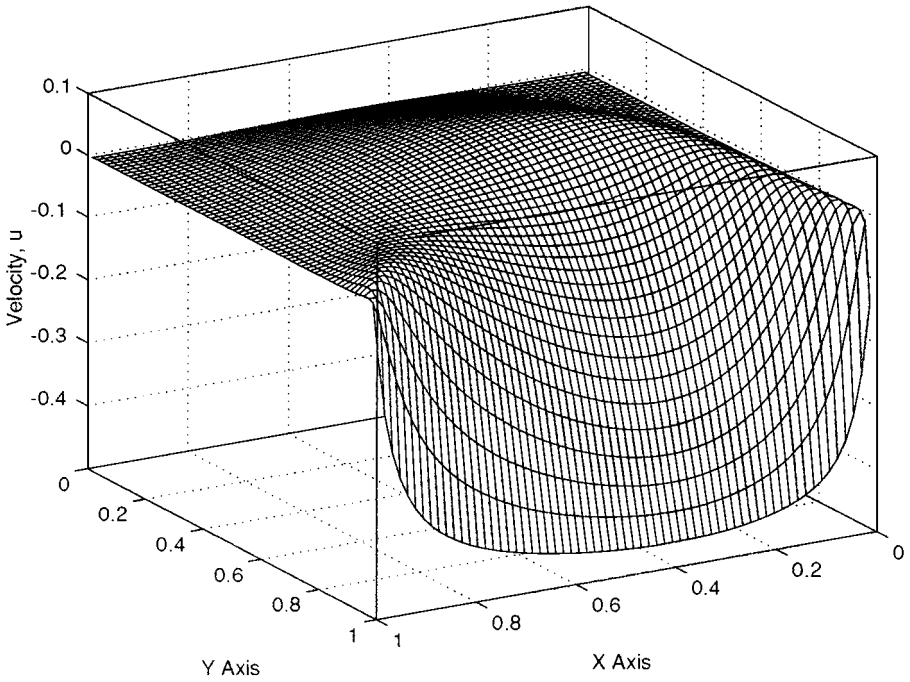

FIG. 11. Variation of the dimensionless u-component of velocity u/c_0 for the KFVS solution to the lid-driven cavity problem. Lid velocity is from left to right on the near face, with $M_{lid} = 0.5$, $Kn_L = 0.01$, and $\gamma = 7/5$.

temperature slip which becomes

$$\left(1 - \frac{1}{2}\hat{\tau}_{nn}^{CE}\right)\frac{T_w}{T_g} = 1 - \left(\frac{\gamma - 1}{\gamma + 1}\right)\left[5\sqrt{\pi}\hat{q}_n^{CE} + \left(\frac{3\gamma - 1}{2(\gamma - 1)} + S_{t1}^2\right)\hat{\tau}_{nn}^{CE}\right] + 2\left(\frac{\gamma - 1}{\gamma + 1}\right)S_{t1}\left[S_{t1} + \sqrt{\pi}\hat{\tau}_{nt1}^{CE} + \hat{q}_{t1}^{CE}\right]. \tag{20}$$

In developing Eq. (20), the coordinate system in which the gas is moving and the wall is stationary was again used. Therefore, a transformation must be introduced when (20) is used to analyze the moving lid. Because of the complexity of (19) and (20), the approach employed in Fig. 1 is less useful here. Here too, Eqs. (19) and (20) can be shown to reduce to Patterson's [9] results.

In the coordinate system defined by Fig. 11, the velocity component u lies parallel to the lid while the velocity component v lies parallel to the two faces on either side of the lid. Therefore, if we unwrap the adjacent faces and display the tangential velocity along the surface as a function of the surface position for the KFVS solution, we obtain the function seen in the top view of Fig. 12, shown as a solid curve. This function contains both u and v and is not merely a copy of the edge values for u shown in Fig. 11. The corresponding theoretical prediction is given by Eq. (19) and is shown as the heavy dotted curve (a transformation must be applied to (19) to obtain the values along the lid). It is clear that agreement is only found outside the two corner regions. This can be understood by reviewing the plot shown in the bottom view of the figure, which gives the normal velocity component S_n as a function of the surface position s. Equation (19) was derived on the basis of the assumption $S_n = 0$ and it is clear from the plot for S_n that the assumption does

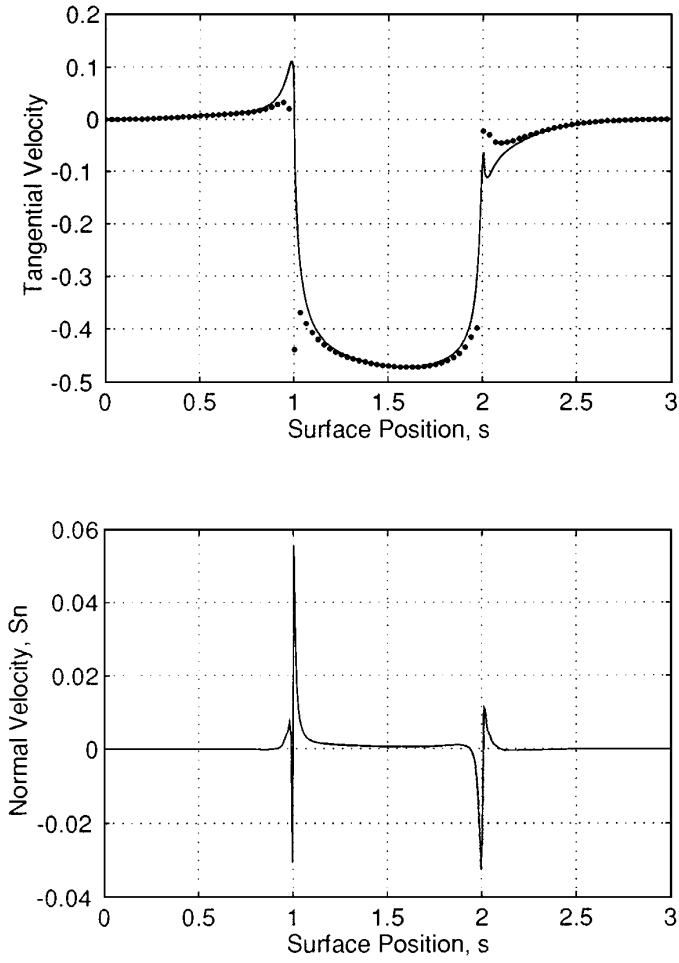

FIG. 12. Dimensionless tangential and normal velocities at the surface of the lid and cavity for the KFVS solution. Upper view: numerical solution of the KFVS equations (solid curve) and the theoretical expression, Eq. (19), for the tangential velocity u_t/c_0 (dotted curve). Lower view: velocity component normal to the surface of the cavity, S_n, for the KFVS solution.

not hold in the two corners. Therefore, use of Eq. (19) as a check on the validity of the numerical solution obtained must be confined to areas near $s = 0.5, 1.5, 2.5$; and this check clearly shows that reliable numerical results were in fact obtained.

Practical considerations made it necessary to limit the DSMC simulation to a 64×64 array of cells. Past experience with the DSMC method led to the decision to use an average number density of approximately 64 particles per cell, leading to a total of roughly 0.25×10^6 particles employed in the simulation. Roughly 12,000 time steps were used in the time averaging of the data which gave a sample size for each cell of approximately 0.75×10^6. The top view of Fig. 13 compares the KFVS solution against DSMC results for the tangential velocity versus the surface position. In each case the data were projected to the position of the surface for comparison. As can be seen, the correspondence is quite complete, even including sharp spikes in the two corners. Consequently, the KFVS prediction for the slip velocity is quite outstanding for these conditions. Because of the low Mach number chosen, $M_{lid} = 0.5$, the temperature rise was fairly small (less than 5%) and the DSMC

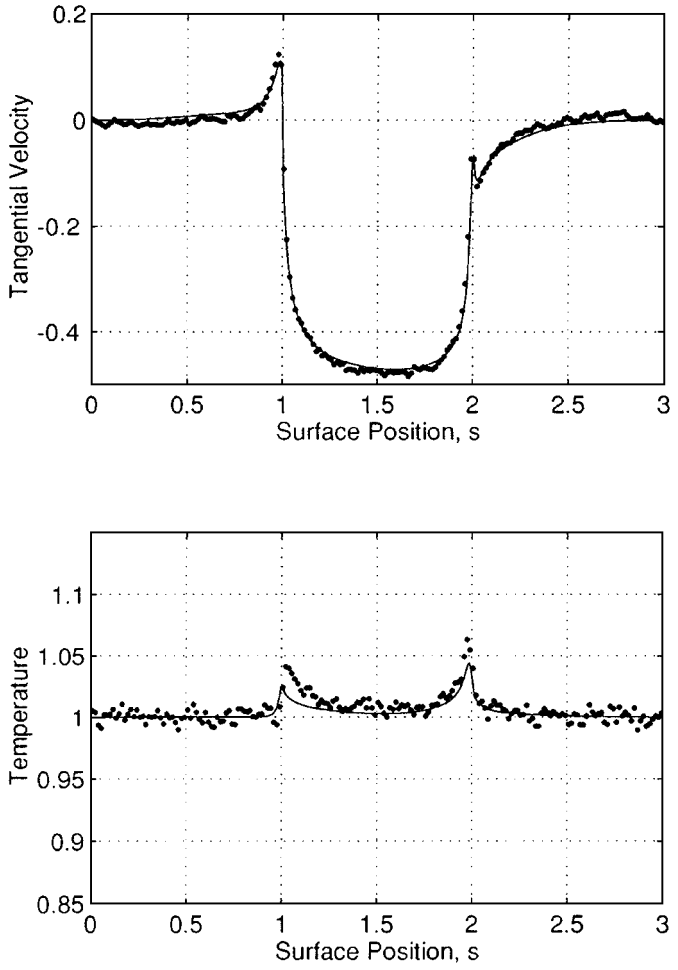

FIG. 13. Tangential velocity, u_t/c_0, and temperature, T/T_0, at the surface of the lid and cavity for the KFVS solution (solid curves) versus result for a DSMC simulation (symbols).

data for temperature exhibit considerable statistical scatter, as is seen in the bottom view in the figure, and a fully equivalent judgment concerning the KFVS temperature slip, DSMC results, and Eq. (20) cannot be made.

Because the wall temperature is specified for an isothermal wall, the KFVS solution only controls the density of the hypothetical wall gas ρ_w (see Eq. (11)). Furthermore, because the emission from the wall is controlled by a Maxwellian distribution in the particular application (isothermal wall) of the KFVS method being considered, the split fluxes directed out of the wall are not overly sensitive to the KFVS solution. Thus, it makes sense to focus attention on the split fluxes directed out of the gas and into the wall. Figure 14 gives a comparison for this single component of the two kinetic split fluxes for energy, where the upper set is for the translational energy component and the lower set is for the rotational energy component. As seen, the KFVS predictions compare extremely well with the DSMC results, including the excursions in the two corners. Likewise, the good match for rotational energy shows that the form of the Eucken approximation employed in the development of the KFVS method proves to be valid even for these conditions.

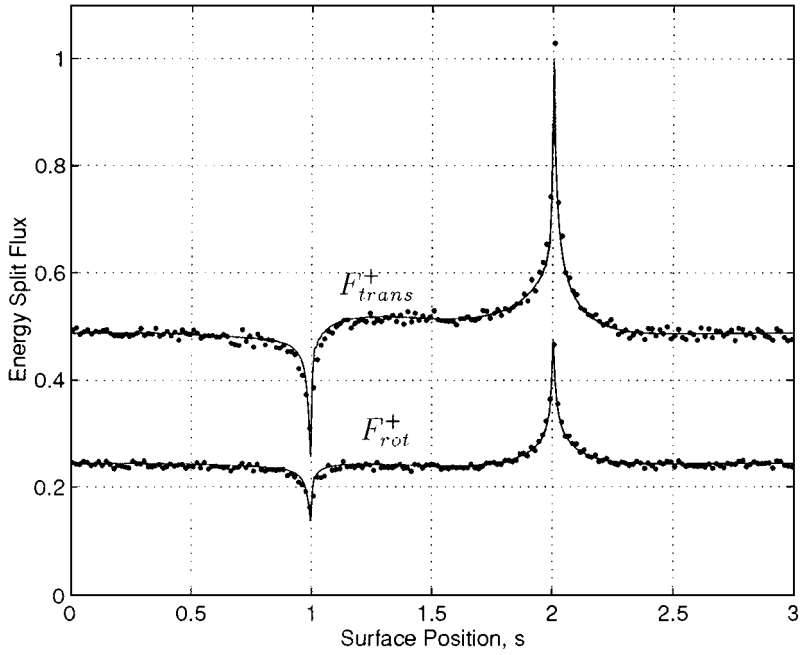

FIG. 14. Translational (upper curves) and rotational (lower curves) energy split fluxes at the surface of the lid and cavity for KFVS (solid curves) and DSMC (symbols). Energy split fluxes are referenced to the value $\rho_0 c_0^3$.

Although prediction of the values of the fluid variables at the lid and walls represents a more severe test of the theory than that for the interior regions of the lid-driven cavity problem, it is also of interest to consider one comparison for the entire flow. Figure 15 displays the v-component of velocity for a number of transverse slices positioned along the x axis. The KFVS solution is given by the solid curves and the DSMC results by the symbols, likewise showing good agreement between the two.

VI. CONCLUDING REMARKS

The method of kinetic flux–vector splitting for the Navier–Stokes equations was introduced primarily as the continuum counterpart to the DSMC method in the eventual development of a hybrid scheme [4]. A principal requirement in joining the two methods at a fluid interface is the presence of compatible split fluxes. Because KFVS is not valid in rarefied flow and the use of the DSMC method becomes overly costly in the deep continuum, matching must be carried out in the near-continuum, where the flow is only slightly rarefied, a degree of rarefaction which may be defined as the regime where the local cell Knudsen number is of order unity. These conditions were considered in selecting the test conditions reported above and very good agreement was found for the split fluxes in the two schemes, even for the extreme nonequilibrium conditions found near isothermal surfaces, conditions surely more severe than those found at most any other interface located in the flow. Because the split fluxes for mass and momentum do not depend on γ, it is certainly expected that one would obtain equally good results for monatomic and diatomic gases for these comparisons. However, the split fluxes for energy clearly depend on the additional internal energy carried by polyatomic molecules and for this case it was necessary to make

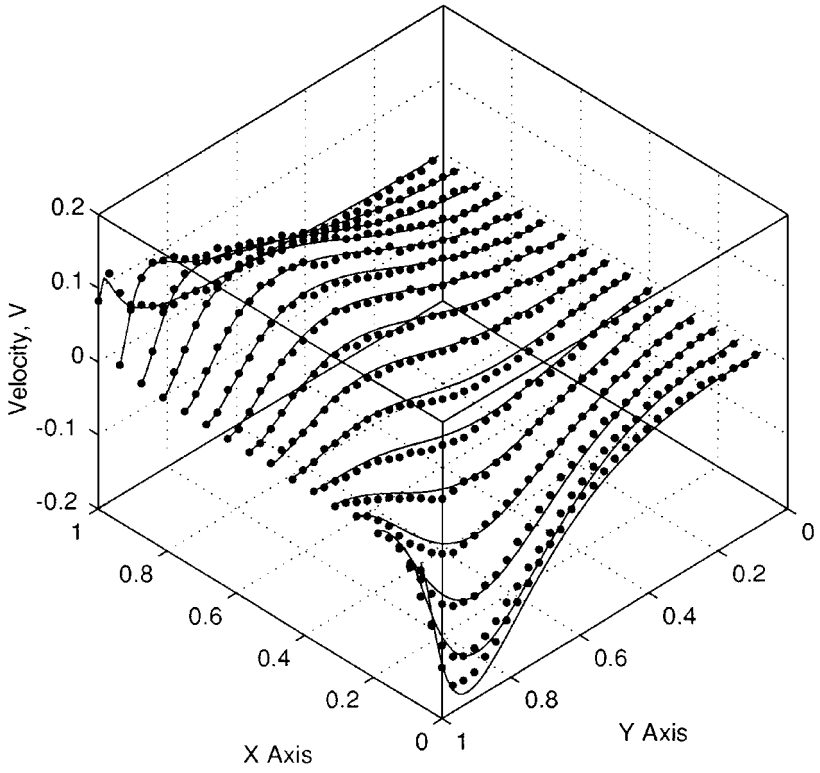

FIG. 15. Comparison of the v-component of velocity, v/c_0, in the cavity for KFVS (solid curves) and DSMC (symbols).

use of a particular interpretation of the Eucken model to carry out the splitting (see Ref. [4]). Therefore, comparisons such as those seen in Figs. 10 and 14 prove to be of great value in justifying the assumptions made. Beyond the fact that the split fluxes defined in KFVS and DSMC have been shown to agree remarkable well, which is an important step in the development of a hybrid scheme, it was also shown that the slip conditions (first-order slip) for temperature and velocity at a material surface also agreed rather well. This is an important result because the flow is fully expected to be slightly rarefied near a material surface for most conditions for which a hybrid scheme would be employed.

ACKNOWLEDGMENTS

This work was supported in part by NASA Grant NCC2-5072. Access to the CACR parallel supercomputer operated by Caltech, on behalf of the Center for Advanced Computing Research, was provided by the Numerical Aerosciences Simulation program at NASA-Ames Research Center.

REFERENCES

1. D. Baganoff and J. McDonald, A collision-selection rule for a particle simulation method suited to vector computers, *Phys. Fluids A* **2**(7), 1248 (1990).
2. G. A. Bird, Monte Carlo simulation to gas flows, *Annu. Rev. Fluid Mech.* **10**, 11 (1978).

3. G. A. Bird, *Molecular Gas Dynamics and the Direct Simulation of Gas Flows* (Clarendon Press, Oxford, 1994).
4. S. Y. Chou and D. Baganoff, Kinetic flux–vector splitting for the Navier–Stokes equations, *J. Comput. Phys.* **130**, 217 (1997).
5. T. J. Denery, *An Extension of the Lees–Liu Solution for Rarefied Couette Flow to General Inverse Power Molecules—Development and Applications*, Ph.D. thesis, Stanford University, 1995.
6. S. M. Deshpande, *Kinetic Theory Based New Upwind Methods for Inviscid Compressible Flows*, AIAA Paper 86-0275 (1986).
7. J. C. Mandal and S. M. Deshpande, Kinetic flux vector splitting for Euler equations, *Comput. & Fluids* **23**, 447 (1994).
8. J. McDonald, *A Computationally Efficient Particle Simulation Method Suited to Vector Computer Architectures*, Ph.D. thesis, Stanford University, 1990.
9. G. N. Patterson, *Molecular Flow of Gases* (Wiley, New York, 1956).
10. D. I. Pullin, Direct simulation methods for compressible inviscid ideal-gas flow, *J. Comput. Phys.* **34**, 231 (1980).
11. V. P. Shidlovskiy, *Introduction to the Dynamics of Rarefied Gases* (American Elsevier, New York, 1967).